Linear Modulation Region Expansion Strategy Based on Voltage Vector Angle Regulation for PMSM Drives With Small DC-Link Capacitor

Runfeng Gao, Dawei Ding, *Member, IEEE*, Gaolin Wang, *Senior Member, IEEE*, Qiwei Wang, *Member, IEEE*, Guoqiang Zhang, *Senior Member, IEEE*, and Dianguo Xu, *Fellow, IEEE*

***Abstract*—Modulation fluctuations will decrease the linear operation range and cause the reduction of dc-link utilization for reduced dc-link capacitance motor drives. In this article, a novel strategy for expanding the linear modulation region based on voltage vector angle regulation is proposed. The phase relationship between the voltage reference and the dc-link voltage fluctuation is carried out creatively to clarify the reduction of linear modulation margin. Based on the impedance matching method, the linear modulation region can be expanded by reducing the phase differences with the regulation of voltage vector angle. According to parameter and performance analysis of the proposed method, the dc-link utilization can be improved by 13.2%. Experimental results validate that the effectiveness of the proposed method.**

***Index Terms*—DC-link voltage fluctuation, linear modulation margin, reduced dc-link capacitance drives, voltage vector angle.**

I. Introduction

PERMANENT magnet synchronous motor (PMSM) has been widely applied in transportation, household appliances and other industrial conditions, which contains advantages, such as convenient control and high power density [1], [2], [3]. The film capacitor is less affected by temperature and can be applied in the dc-link to improve the system lifetime [4], reduce the volume and enhance the reliability through eliminating the power factor correction circuit and reducing the system size [4], [5], [6]. In recent years, many researches have paid attention to reduced capacitance drivers in the industrial applications such as the commercial air-conditioners and the integrated pumping [4], [5], [6]. However, the decrease of dc-link capacitance will lead the dc-link power difficult to be maintained, which aggravate the energy coupling between the grid and the motor sides. The dc-link voltage and the grid current are inevitably introduced significant fluctuation. Hence, some challenges occur, such as the deterioration of dc-link utilization [7], [8].

The dc-link voltage utilization determines the voltage output capacity of the motor, whose control is a key technology in the drive system with small dc-link capacitors [9]. Usually, PMSM can be regarded as a constant power load, which will aggravate the stability problem and introduce the additional ripples into the dc-link voltage [10]. The dc-link voltage fluctuation generates additional harmonics into the total dwell time of voltage vectors, which causes the system to enter the overmodulation region earlier [11], [12]. The reduction of the linear modulation margin will import additional ripples into the motor voltage and results in the reduction of voltage utilization [12]. The utilization of dc-link voltage is necessary to prevent the motor voltage output of the drive system from being saturated [13]. Hence, some effective methods have been proposed to improve the motor side performance and the utilization of dc-link voltage.

Generally, the improvement methods for dc-link utilization can be divided into two categories [14], the hardware topology methods [13], [14] and advanced control methods [15], [16]. The hardware methods vary the topologies of drive, which have the characteristics of robustness. In [17], a nine-switch boost inverter (NSBI) for multiphase drives was applied to replace the conventional voltage-source inverter. Compared with other topologies, the NSBI requires less input dc-link voltage to drive the motor. In [18], the required technology and construction features of the solid-state transformers were designed to improve the output ability of dc-link side, which can further increase the stability and economic operation of drive systems. In [19], a single dc source-based hybrid three-phase inverter was proposed, which possessed optimal switch count and high dc-link voltage utilization. In [20], a fault-tolerant multiphase multilevel inverter (MPMLI) configuration was proposed to improve the output performance in normal and failure condition. Compared with other inverters, the MPMLI can drive the PMSM with less dc-link voltage under the same operation condition. However, the above methods were realized through adding additional power electronic devices, which increases the volume and cost of the system [21].

Compared with the hardware topology methods, the advanced control strategies do not require additional devices, and have the advantage of more flexibility. In [22], the finite control set model predictive control was improved only using the large vectors

Manuscript received 23 November 2022; revised 2 February 2023; accepted 2 April 2023. Date of publication 17 April 2023; date of current version 19 May 2023. This work was supported in part by the Research Fund for the National Natural Science Foundation of China under Grants 52207042, 52125701, and 52177034 and in part by the fellowship of China Postdoctoral Science Foundation under Grant 2022M720946. Recommended for publication by Associate Editor K. Akatsu. *(Corresponding author: Dawei Ding.)*

The authors are with the School of Electrical Engineering and Automation, Harbin Institute of Technology, Harbin 150001, China (e-mail: 1160800915@stu.hit.edu.cn; dingdawei@hit.edu.cn; wgl818@hit.edu.cn; wqw0543@163.com; zhgq@hit.edu.cn; xudiang@hit.edu.cn).

Color versions of one or more figures in this article are available at https://doi.org/10.1109/TPEL.2023.3267780.

Digital Object Identifier 10.1109/TPEL.2023.3267780

to evaluate the cost function, which can reduce common-mode voltage and increase the margin of output voltage. In [23], a unique method based on the injection of zero-sequence voltage harmonics was applied in the sliding mode control of PMSM drive, which increases the voltage utilization by 15%. An inverter control method based on enhanced virtual synchronous machine (eVSM) was proposed in [24]. The drive system with eVSM can obviate the need for large dc-link capacitance. In order to improve the utilization and dynamic performance under the fluctuated dc-link voltage, a direct instantaneous power predictive control method was proposed through the power analysis in [25].

The above strategies are mainly applied to the large dc-link capacitance drive in which the dc-link voltage fluctuation is lower [26], [27]. In the drive system with slim film capacitors, the serious ripples of the dc-link voltage introduce additional fluctuation to the modulation module, which leads the distortion of motor voltage [28], [29]. Hence, the feedback from the instantaneous value of dc-link voltage is widely applied in the vector modulation strategy, which can be mainly applied for active damping schemes [30], [31] and flux-weakening schemes [11], [33]. In [30], the damping voltage command could be generated by the dc-link voltage, which was injected into the voltage vector command to ensure the suppression effect of grid harmonics. In [31], the harmonics of dc-link voltage at specific frequencies was regulated according to the impedance analysis, which aimed to improve the power quality of grid current. However, active damping methods for stability control are usually applied through varying the amplitude of the voltage vector, which further decreases the dc-link voltage utilization [30], [31]. Therefore, more effective methods are required to expand the linear modulation region and improve the dc-link utilization [32]. In [33], the dc-link voltage closed-loop was combined with the adaptive fuzzy logic speed controller, which could prevent the influence of dc-link ripple on the dc-link utilization. In [11], a field-weakening method based on a closed-loop of dc-link voltage with adjustable maximum voltage margin was proposed. The torque and speed fluctuation can be reduced by 85%, which ameliorate the voltage utilization. In [12], the voltage reference of space vector pulse width modulation (SVPWM) was switched between the actual dc-link voltage and the fixed voltage to reduce the additional harmonics of motor voltages and currents. However, these methods are difficult to be applied directly for enhancing the dc-link utilization in the linear modulation region.

In this article, a novel linear modulation region expansion strategy based on the voltage vector angle regulation is proposed for PMSM drive with small film capacitors to improve the voltage utilization. According to an impedance model of the system, the phase difference between the voltage vector harmonics and the dc-link voltage harmonics at the same frequency is derived, which explains the generation of modulation index harmonics in linear modulation region. Based on an impedance matching method, the modulation index harmonics can be suppressed through regulating the phase differences, which further improves the dc-link utilization by 13.2% in liner modulation region. Compared with the existing solutions [22], [23], [24], [25], the equivalent regulated signal on the voltage reference can vary adaptively with the operation condition. Experimental verification is carried out on an electrolytic capacitorless PMSM drive.

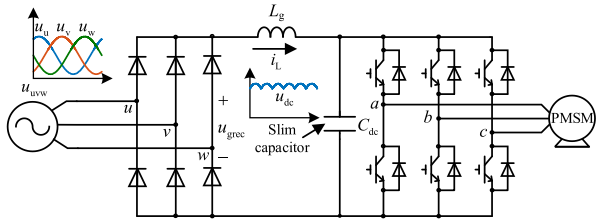

Fig. 1. Topology of the three-phase PMSM drives with slim film capacitors.

II. Influence of Reduced DC-Link Capacitance on Inverter Modulation

A. Modulation Harmonics Caused By DC-link Fluctuation

The topology of the three-phase input PMSM drive with slim film capacitors is shown in Fig. 1. Due to the use of slim film dc-link capacitor, the dc-link voltage $u_{\rm dc}$ cannot be maintained as a constant value, which can be denoted as

$$u_{\rm dc} = U_{\rm dc,0} + \sum_{k=1}^{\infty} U_{\rm dc,k} \sin\left(6k\omega_{\rm g} t + \varphi_{\rm k}\right) \tag{1}$$

where $U_{\rm dc,0}$ is the average value of the dc-link voltage, $U_{{\rm dc},k}$ and φ_k are the amplitude and phase of kth harmonics, ω_g is the angular frequency of the grid voltage. It can be seen that the dc-link voltage fluctuates with six times the frequency of the grid voltage.

In SVPWM, $\boldsymbol{u}_{\rm sref}$ is composed of a zero vector and two adjacent basic voltage vectors. The total dwell time of basic voltage vectors in one sector can be expressed as

$$T_v = T_i + T_{i+1} = \frac{\sqrt{3}\left|\boldsymbol{u}_{\rm sref}\right| T_s}{u_{\rm dc\_}s} \sin\left[\boldsymbol{M}\left(\theta_u, \frac{\pi}{3}\right) + \frac{\pi}{3}\right] \tag{2}$$

where T_i and T_{i+1} are the dwell time of two basic voltage vectors in the ith sector, respectively. T_v is the total dwell time, $T_{\rm s}$ is the switching period. $u_{{\rm dc}\_s}$ is the sampled dc-link voltage, θ_u is the angle of the voltage vector reference. $\boldsymbol{M}(x, y)$ is the function of obtaining the remainder of x divided by y.

The total dwell time T_v remains consistent in each sector. Hence, its fundamental frequency is six times of the frequency of voltage vector according to (2). Assuming the initial phase is zero, the fast Fourier transform of T_v can be presented as

$$T_v = \frac{3\sqrt{3}\left|\boldsymbol{u}_{\rm sref}\right| T_s}{\pi u_{\rm dc\_}s} - \sum_{n=1}^{\infty} \frac{6\sqrt{3}\left|\boldsymbol{u}_{\rm sref}\right| T_s}{\pi(36k^2-1)u_{\rm dc\_}s} \cos(6k\omega_e t). \tag{3}$$

where ω_e is the angular frequency of the voltage vector.

Due to the large periodical fluctuations in the dc-link voltage, harmonics at the same frequencies may emerge in the motor voltage. Hence, the modulation index m is obtained as

$$m = \frac{\sqrt{3}\left|\boldsymbol{u}_{\rm sref}\right|}{u_{\rm dc\_}s} = M_0 + \sum_{k=1}^{\infty} M_k \sin(6k\omega_g t + \varphi_{gk}) \tag{4}$$

where M_0, M_k, and φ_{gk} are the average value of the modulation index, the amplitude, and phase of kth harmonics, respectively.

According to (3) and (4), the total dwell time will fluctuate due to the dc-link voltage, and harmonics at the frequency of $6k\omega_g$, $6(k_2\omega_g\text{-}k_1\omega_e)$, and $6(k_2\omega_g{+}k_1\omega_e)$, which can be expressed as (5). This phenomenon will reduce the voltage utilization of the drive, since the system is more likely to enter the overmodulation region

$$\frac{T_v}{T_s} = \sum_{k=1}^{\infty}\frac{3M_k}{\pi}\sin(6k\omega_g t+\varphi_{gk}) - \sum_{k=1}^{\infty}\frac{6M_0\cos(6k\omega_e t)}{\pi(36k^2-1)} - \sum_{k_1=1}^{\infty}\sum_{k_2=1}^{\infty}\frac{3M_{k_2}/\pi}{(36k_1^2-1)}\{\sin[6(k_2\omega_g+k_1\omega_e)t+\varphi_{gk_2}] + \sin[6(k_2\omega_g-k_1\omega_e)t+\varphi_{gk_2}]\} + 3M_0/\pi. \quad (5)$$

According to [12], the fluctuation of the basic vector causes the size of the voltage boundary hexagon to vary with the fluctuation on the dc-link voltage. In order to get rid of the influence of the dc-link fluctuation, a modulation vector $\boldsymbol{m}$ is defined as

$$\boldsymbol{m} = \frac{\sqrt{3}\boldsymbol{u}_{\text{sref}}}{u_{\text{dc\_}s}} = \frac{\sqrt{3}u_{\alpha\text{ref}}}{u_{\text{dc\_}s}} + j\frac{\sqrt{3}u_{\beta\text{ref}}}{u_{\text{dc\_}s}} = m_\alpha + jm_\beta \quad (6)$$

where $u_{\alpha\text{ref}}$, $u_{\beta\text{ref}}$, m_α, and m_β are the reference voltages and modulation index in $\alpha\beta$-axes, respectively.

According to (6), the amplitude of the basic modulation vector is a constant value, which means that the modulation boundary hexagon is fixed as the dc-link voltage fluctuates. From (2), the maximum modulation index m_{li} in the linearly modulated system satisfies

$$m_{li} = \frac{1}{\sin[\boldsymbol{M}(\theta_u,\pi/3)+\pi/3]}. \quad (7)$$

In this article, an indicator named the linear modulation margin M_{mar} is defined as (8) to show the modulation region, which can be regarded as the distance between the modulation boundary hexagon and the operation area of modulation vector

$$M_{\text{mar}} = m_{li} - m = \frac{1}{\sin[\boldsymbol{M}(\theta_u,\pi/3)+\pi/3]} - \left[M_0 + \sum_{k=1}^{\infty}M_k\sin(6k\omega_g t+\varphi_{gk})\right]. \quad (8)$$

According to (8), the linear modulation margin with different modulation conditions is shown in Fig. 2. The system is located in linear modulation region if M_{mar} is larger than zero, which is shown in Fig. 2(a). Otherwise, SVPWM enters the overmodulation mode, which is shown in Fig. 2(b).

The influence of the dc-link voltage fluctuation on the modulation index can be demonstrated as shown in Fig. 3(a). Due to the wide-range fluctuations of the modulation index, SVPWM will enter the overmodulation region earlier. The linear modulation margin under different voltage vector angles and harmonic amplitudes of the dc-link voltage are shown in Fig. 3(b). As can be seen, the linear modulation margin varies in a wide range with different angles of voltage vector. For example, the system will

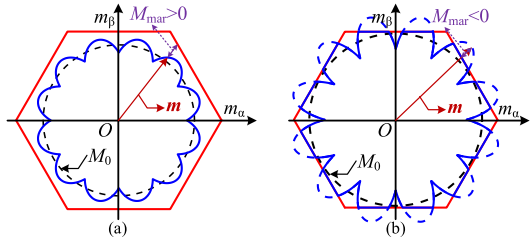

Fig. 2. Linear modulation margin with different modulation conditions. (a) Linear modulation. (b) Over modulation.

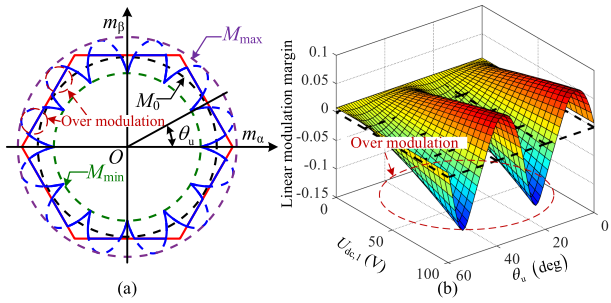

Fig. 3. Modulation index under fluctuated DC-link voltage. (a) Schematic diagram in over modulation region. (b) Linear modulation margin.

locate in overmodulation even if $U_{\text{dc},1}$ is small, when θ_u is 20°. The situation is revised if θ_u is 35°, the system is always located in linear modulation region. The phenomenon shows that, the investigation of the angle of the voltage vector is necessary to improve the liner modulation margin.

The linear modulation margin can be simplified as the minimum value, which is denoted as

$$M_{\text{mar}} = \left\{\frac{1}{\sin[\boldsymbol{M}(\theta_u,\pi/3)+\pi/3]} - m\right\}_{\min} = 1 - M_{\max} \quad (9)$$

where $M_{\max}$ is the maximum modulation index.

According to (9), the drive system is linearly modulated as the linear modulation margin is lower than zero. The reduction of the linear modulation margin will introduce additional fluctuation into the voltage vector. The distortion of the voltage vector will reduce M_0, which means the fundamental voltage at linear modulation is smaller and the dc-link utilization is lower.

B. Analysis of Linear Modulation Margin Based on Impedance Model

In order to figure out the quantitative influence of modulation index harmonics caused by the dc-link voltage fluctuation, the small-signal model of drive system is carried out. The motor voltages in dq-axes are related to the voltage command and the dc-link voltage [30], [31]. The relationship between the actual and the reference voltages can be yielded

$$\begin{bmatrix}u_d\\u_q\end{bmatrix} = \frac{u_{\text{dc}}}{u_{\text{dc\_}e}}\begin{bmatrix}u_{d\text{ref}}\\u_{q\text{ref}}\end{bmatrix} = \frac{U_{\text{dc},0}+\Delta u_{\text{dc}}}{U_{\text{dc},0}+e^{-1.5sT_s}\Delta u_{\text{dc}}}\begin{bmatrix}u_{d\text{ref}}\\u_{q\text{ref}}\end{bmatrix} \quad (10)$$

where u_{dc_e} is the equivalent sampled dc-link voltage, Δu_{dc} is the small signal variations of the dc-link voltage, $u_{d,q}$ and $u_{d,q\text{ref}}$ are the actual and the reference voltages in dq-axes, respectively.

According to (10), the small signal variations of the actual voltages $\Delta u_{d,q}$ can be expressed as

$$\begin{bmatrix}\Delta u_d\\ \Delta u_q\end{bmatrix} = \begin{bmatrix}\Delta u_{d\text{ref}}\\ \Delta u_{q\text{ref}}\end{bmatrix} + \frac{\left(1-e^{-1.5sT_s}\right)\Delta u_{\text{dc}}}{U_{\text{dc},0}}\begin{bmatrix}U_{d\text{ref},0}\\ U_{q\text{ref},0}\end{bmatrix} \tag{11}$$

where $U_{d\text{ref},0}$, $U_{q\text{ref},0}$, $\Delta u_{d\text{ref}}$, and $\Delta u_{q\text{ref}}$ are the averages and the small signal variations of the reference voltage in dq-axes, respectively.

As can be seen in (11), the fluctuated dc-link voltage will cause additional harmonics in the motor voltage. For system modeling, the motor side should be taken into consideration as well. According to the voltage equations of the motor, the small signal model of the motor can be denoted as

$$\begin{bmatrix}\Delta u_d\\ \Delta u_q\end{bmatrix} = \begin{bmatrix}R_s+L_ds & -\omega_eL_q\\ \omega_eL_d & R_s+L_qs\end{bmatrix}\begin{bmatrix}\Delta i_d\\ \Delta i_q\end{bmatrix} \tag{12}$$

where L_d, L_q, and R_s, are the dq-axes inductances and the stator resistance, respectively, Δi_d and Δi_q are the small signal variations of actual currents in dq-axes.

As for vector control system, the reference voltages are generated by the current controllers, which can be presented as

$$\begin{bmatrix}u_{d\text{ref}}(s)\\ u_{q\text{ref}}(s)\end{bmatrix} = \begin{bmatrix}-\boldsymbol{G}_d & -\omega_eL_q\\ \omega_eL_d & -\boldsymbol{G}_q\end{bmatrix}\begin{bmatrix}i_d(s)\\ i_q(s)\end{bmatrix} + \begin{bmatrix}\boldsymbol{G}_di_{d\text{ref}}(s)\\ \boldsymbol{G}_qi_{q\text{ref}}(s)\end{bmatrix} \tag{13}$$

where $\boldsymbol{G}_d$, $\boldsymbol{G}_q$, $i_{d\text{ref}}$, $i_{q\text{ref}}$, i_d, and i_q are the transfer functions of current controllers, the reference and the actual currents in dq-axes, respectively.

The transfer function of the current controllers can be presented as

$$\boldsymbol{G}_d = K_{pd} + \frac{K_{id}}{s}, \boldsymbol{G}_q = K_{pq} + \frac{K_{iq}}{s} \tag{14}$$

where K_{pd}, K_{pq}, K_{id}, and K_{iq} are the proportional and integral gains of the current controllers, respectively.

Generally, the bandwidth of the speed loop is one tenth of that of current loop. Hence, the small signal variations of reference currents can be regarded as 0. The reference voltages can be expressed as

$$\begin{bmatrix}\Delta u_{d\text{ref}}(s)\\ \Delta u_{q\text{ref}}(s)\end{bmatrix} = \begin{bmatrix}-\boldsymbol{G}_d & -\omega_eL_q\\ \omega_eL_d & -\boldsymbol{G}_q\end{bmatrix}\begin{bmatrix}\Delta i_d(s)\\ \Delta i_q(s)\end{bmatrix}. \tag{15}$$

From (11), (12), and (15), the transfer function between the stator currents and the dc-link voltage can be presented as

$$\begin{bmatrix}\boldsymbol{W}_d(s)\\ \boldsymbol{W}_q(s)\end{bmatrix} = \begin{bmatrix}\frac{\Delta i_d}{\Delta u_{\text{dc}}}\\ \frac{\Delta i_q}{\Delta u_{\text{dc}}}\end{bmatrix} = \frac{1-e^{-1.5sT_s}}{U_{\text{dc},0}}\begin{bmatrix}\frac{U_{d\text{ref},0}}{R_s+L_ds+\boldsymbol{G}_d}\\ \frac{U_{q\text{ref},0}}{R_s+L_qs+\boldsymbol{G}_q}\end{bmatrix} \tag{16}$$

where $\boldsymbol{W}_d(s)$ and $\boldsymbol{W}_q(s)$ are the transfer functions between $\Delta i_{d,q}$ and Δu_{dc}, respectively.

According to (15) and (16), the relationship between the reference voltage and the dc-link voltage are expressed as

$$\begin{bmatrix}\Delta u_{d\text{ref}}(s)\\ \Delta u_{q\text{ref}}(s)\end{bmatrix} = \Delta u_{\text{dc}}\begin{bmatrix}-\boldsymbol{G}_d\boldsymbol{W}_d(s)-\omega_eL_q\boldsymbol{W}_q(s)\\ \omega_eL_d\boldsymbol{W}_d(s)-\boldsymbol{G}_q\boldsymbol{W}_q(s)\end{bmatrix}. \tag{17}$$

Then, the amplitude of voltage vector reference can be expressed as

$$|\boldsymbol{u}_{\text{sref}}| = \sqrt{u_{d\text{ref}}^2+u_{q\text{ref}}^2}. \tag{18}$$

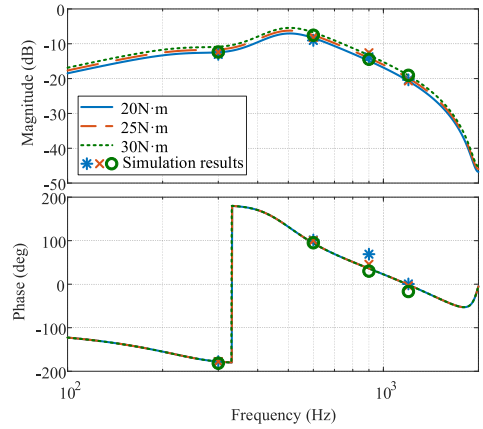

Fig. 4. Bode diagrams of $\boldsymbol{G}_s(s)$ under different torques.

By linearizing (18), the small signal variation of the voltage vector reference can be presented as

$$\Delta|\boldsymbol{u}_{\text{sref}}| \approx \frac{U_{d\text{ref},0}\Delta u_{d\text{ref}} + U_{q\text{ref},0}\Delta u_{q\text{ref}}}{U_{\text{sref},0}} \tag{19}$$

where $\Delta|\boldsymbol{u}_{\text{sref}}|$ is the small signal variation of the amplitude of voltage vector reference, $U_{\text{sref},0}$ is the average of the amplitude of voltage vector reference.

Combining (17) with (16) and (19), the transfer function $\boldsymbol{G}_{\text{s}}(s)$ between the voltage vector reference and the dc-link voltage can be expressed as

$$\boldsymbol{G}_{\text{s}}(s) = \frac{\Delta|\boldsymbol{u}_{\text{sref}}|}{\Delta u_{\text{dc}}} = \left[\frac{U_{d\text{ref},0}\left(\omega_eL_dU_{q\text{ref},0}-U_{d\text{ref},0}\boldsymbol{G}_d\right)}{R_s+L_ds+\boldsymbol{G}_d} - \frac{U_{q\text{ref},0}\left(\omega_eL_qU_{d\text{ref},0}+U_{q\text{ref},0}\boldsymbol{G}_q\right)}{R_s+L_qs+\boldsymbol{G}_q}\right]\frac{1-e^{-1.5sT_s}}{U_{\text{sref},0}U_{\text{dc},0}}. \tag{20}$$

Setting the motor speed at 60 Hz, the Bode diagrams of $\boldsymbol{G}_s(s)$ under different torques are shown in Fig. 4. It can be seen that, the magnitude of the impedance model is approximately consistent with that of simulation results at the frequencies of $6\omega_g$ and $12\omega_g$. In this article, the grid voltage is 380 V, 50 Hz. Besides, the phase difference between the voltage vector harmonics and the dc-link voltage harmonics is 180° at the frequency of $6\omega_g$, which means the maximum value of the voltage vector reference and the minimum value of the dc-link voltage appears at the same time.

The relationship among linear modulation margin with different phase differences of the harmonics in u_{dc} and $|\boldsymbol{u}_{\text{sref}}|$ is shown in Fig. 5. The modulation fluctuation increases to the maximum value when the phase error is 180°, which deteriorates the linear modulation margin. That means the dc-link voltage utilization will be reduced as analyzed in Fig. 2. Hence, it is necessary to suppress the modulation index fluctuation by adjusting the phase difference.

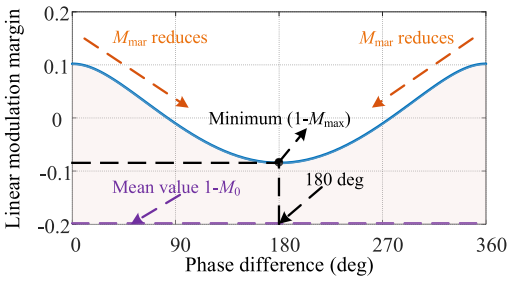

Fig. 5. Linear modulation margin under different phase errors.

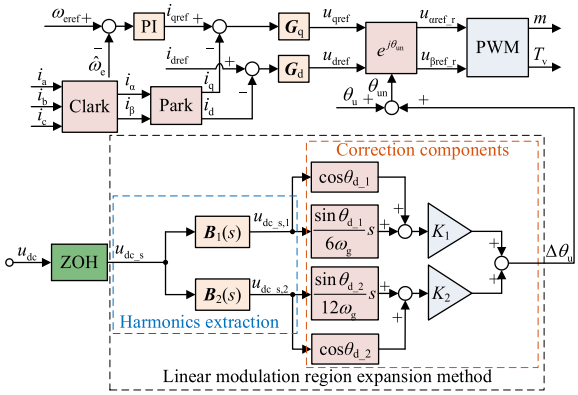

Fig. 6. Block diagram of the proposed linear modulation region expansion method.

III. Proposed Linear Modulation Region Expansion Strategy

A. Scheme of Voltage Vector Angle Regulation

According to the above analysis, the modulation index fluctuation is occurred due to the phase difference between the voltage vector harmonics and the dc-link voltage harmonics at the same frequency. Hence, the harmonics of modulation index can be suppressed through adjusting the phase difference at the frequencies of $6\omega_g$ and $12\omega_g$. Thus, a linear modulation expansion strategy is proposed by only manipulating the angle of the voltage vector reference, which is shown in Fig. 6. The regulated angle $\Delta\theta_u$ can be constructed by the amplitude and phase of the extracted dc-link voltage harmonics through the correction components $\boldsymbol{M}_{d\_1}(s)$ and $\boldsymbol{M}_{d\_2}(s)$. The voltage references in $\alpha\beta$-axes are generated by the modified voltage angle.

Considering that the modulation index harmonics at the frequencies of $6\omega_g$ and $12\omega_g$ are the main reasons for the reduction of the linear modulation margin, the angle of the voltage vector reference θ_u is superimposed with the addition harmonics at the same frequencies, which is expressed as

$$\begin{aligned}\theta_{un} &= \theta_u + \Delta\theta_u = \theta_u + \Delta\theta_{u1} + \Delta\theta_{u2} \\ &= \theta_u + A_6\sin(6\omega_g t + \varphi_{u6}) + A_{12}\sin(12\omega_g t + \varphi_{u12})\end{aligned} \tag{21}$$

where θ_{un} and $\Delta\theta_u$ are the voltage angle after regulation and the regulated angle, $\Delta\theta_{u1}$ and $\Delta\theta_{u2}$ are the harmonics of regulated

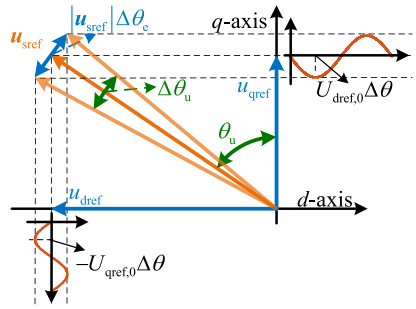

Fig. 7. Schematic diagram of voltage space vector angle regulation.

angle at the frequencies of $6\omega_g$ and $12\omega_g$, A_6, A_{12}, φ_{u6} and φ_{u12} are the amplitudes and phases of the harmonics of $\Delta\theta_{u1}$ and $\Delta\theta_{u2}$, respectively.

The equivalent reference voltages u_{dref_r} and u_{qref_r} are illustrated in Fig. 7, which can be expressed as

$$\begin{cases} u_{dref\_r} = |\boldsymbol{u}_{sref}|\cos(\theta_u + \Delta\theta_u) \\ u_{qref\_r} = |\boldsymbol{u}_{sref}|\sin(\theta_u + \Delta\theta_u) \end{cases}. \tag{22}$$

From (22), the relationship between the voltage references in dq-axes with and without the strategy can be presented as

$$\begin{bmatrix} U_{dref\_r,0} + \Delta u_{dref\_r} \\ U_{qref\_r,0} + \Delta u_{qref\_r} \end{bmatrix} = \begin{bmatrix} \cos\Delta\theta_u & -\sin\Delta\theta_u \\ \sin\Delta\theta_u & \cos\Delta\theta_u \end{bmatrix} \begin{bmatrix} u_{dref} \\ u_{qref} \end{bmatrix} \tag{23}$$

where $U_{dref\_r,0}$, $U_{qref\_r,0}$, Δu_{dref_r}, and Δu_{qref_r} are the averages and small signal variations of the equivalent reference voltages, respectively.

The amplitudes of the regulated angle A_6 and A_{12} are small enough compared with the voltage angle. According to the Bessel function [34], (23) can be rewritten as

$$\begin{bmatrix} U_{dref\_r,0} + \Delta u_{dref\_r} \\ U_{qref\_r,0} + \Delta u_{qref\_r} \end{bmatrix} = \begin{bmatrix} U_{dref,0} + \Delta u_{dref} - U_{qref,0}\Delta\theta_u \\ U_{qref,0} + \Delta u_{qref} + U_{dref,0}\Delta\theta_u \end{bmatrix}. \tag{24}$$

As shown in Fig. 7 and (24), the regulation of voltage angle is equivalent to introduce additional small-signal voltages in dq-axes. The amplitude of the introduced small-signal voltages in d-axis and q-axis can vary adaptively with the operation condition.

The regulated angle can be generated from the harmonics at the frequencies of $6\omega_g$ and $12\omega_g$ from the sampled dc-link volage. The harmonics of dc-link voltage $u_{dc\_s,1}$ and $u_{dc\_s,2}$ can be extracted by two band-pass filters BPF1 and BPF2, whose center frequencies are $6\omega_g$ and $12\omega_g$, respectively. They can be expressed as

$$\begin{cases} u_{dc\_s,1} = U_{dc,1}\sin(6\omega_g t + \varphi_1 - 3\omega_g T_s) \\ u_{dc\_s,2} = U_{dc,2}\sin(12\omega_g t + \varphi_2 - 6\omega_g T_s) \end{cases}. \tag{25}$$

The transfer functions of BPF1 and BPF2 are expressed as

$$\begin{cases} \boldsymbol{B}_1(s) = \frac{6\xi_1\omega_g s}{s^2 + 6\xi_1\omega_g s + 36\omega_g^2} \\ \boldsymbol{B}_2(s) = \frac{12\xi_2\omega_g s}{s^2 + 12\xi_2\omega_g s + 144\omega_g^2} \end{cases} \tag{26}$$

where $\boldsymbol{B}_1(s)$ and $\boldsymbol{B}_2(s)$ are the transfer functions of the band-pass filters, ξ_1 and ξ_2 are the bandwidths of BPF1 and BPF2, respectively.

In order to generate the regulation angle in (21) with the voltage harmonics in (25), the transfer functions of the correction components should be matched

$$\boldsymbol{M}_{d\_1}(s)=\frac{\boldsymbol{L}(\Delta\theta_{u1})}{\boldsymbol{L}(u_{\mathrm{dc\_}s,1})},\boldsymbol{M}_{d\_2}(s)=\frac{\boldsymbol{L}(\Delta\theta_{u2})}{\boldsymbol{L}(u_{\mathrm{dc\_}s,2})} \tag{27}$$

where $\boldsymbol{M}_{d\_1}(s)$ and $\boldsymbol{M}_{d\_2}(s)$ are the transfer functions of correction components, $\boldsymbol{L}(\cdot)$ is the Laplace transformation.

According to the frequency characteristics of $\boldsymbol{M}_{d\_1}(s)$ and $\boldsymbol{M}_{d\_2}(s)$ as shown in (A1), the transfer functions of the correction components can be expressed as

$$\begin{cases}\boldsymbol{M}_{d\_1}(s)=K_1\left(\cos\theta_{\mathrm{d\_1}}+\frac{\sin\theta_{d\_1}}{6\omega_g}s\right)\\ \boldsymbol{M}_{d\_2}(s)=K_2\left(\cos\theta_{\mathrm{d\_2}}+\frac{\sin\theta_{d\_2}}{12\omega_g}s\right)\end{cases}. \tag{28}$$

Then, the regulation angle can be expressed as

$$\begin{aligned}\Delta\theta_u(s)&=\boldsymbol{M}_{d\_1}\boldsymbol{B}_1(s)u_{\mathrm{dc\_}s}\\&\quad+\boldsymbol{M}_{d\_2}\boldsymbol{B}_2(s)u_{\mathrm{dc\_}s}=\boldsymbol{G}_{\mathrm{mad}}(s)u_{\mathrm{dc}}\end{aligned} \tag{29}$$

where $\boldsymbol{G}_{\mathrm{mad}}(s)$ is the transfer function between the regulated angle and the dc-link voltage.

B. Parameter and Performance Analysis of the Proposed Method

In order to obtain the optimal control effect, the parameters of correction components need to be analyzed. The impedance model after applying the method is applied to analyze the harmonics of modulation index, which can be regarded as the basis for parameter design. Substituting (24) into (11), the small signal variations of the actual voltage in *dq*-axes with the proposed strategy can be expressed as

$$\begin{aligned}\begin{bmatrix}\Delta u_d\\ \Delta u_q\end{bmatrix}&=\begin{bmatrix}\Delta u_{d\mathrm{ref}}-U_{q\mathrm{ref},0}\Delta\theta_u\\ \Delta u_{q\mathrm{ref}}+U_{d\mathrm{ref},0}\Delta\theta_u\end{bmatrix}\\&\quad+\frac{\left(1-e^{-1.5sT_s}\right)\Delta u_{\mathrm{dc}}}{U_{\mathrm{dc},0}}\begin{bmatrix}U_{d\mathrm{ref},0}\\ U_{q\mathrm{ref},0}\end{bmatrix}.\end{aligned} \tag{30}$$

According to (15) and (30), (16) can be represented as (31) after using the proposed strategy

$$\begin{bmatrix}\boldsymbol{W}_{d\mathrm{mad}}\\ \boldsymbol{W}_{q\mathrm{mad}}\end{bmatrix}=\begin{bmatrix}\boldsymbol{W}_d\\ \boldsymbol{W}_q\end{bmatrix}+\boldsymbol{G}_{\mathrm{mad}}\begin{bmatrix}\frac{-U_{q\mathrm{ref},0}}{R_s+L_ds+\boldsymbol{G}_d}\\ \frac{U_{d\mathrm{ref},0}}{R_s+L_qs+\boldsymbol{G}_q}\end{bmatrix} \tag{31}$$

where $\boldsymbol{W}_{d\mathrm{mad}}(s)$ and $\boldsymbol{W}_{q\mathrm{mad}}(s)$ are the transfer functions between $\Delta i_{d,q}$ and Δu_{dc} after applying the linear modulation expansion method.

Then the ratio of the equivalent reference voltages and the dc-link voltage can be expressed as

$$\begin{aligned}\begin{bmatrix}\Delta u_{d\mathrm{ref}\_r}/\Delta u_{\mathrm{dc}}\\ \Delta u_{q\mathrm{ref}\_r}/\Delta u_{\mathrm{dc}}\end{bmatrix}&=\begin{bmatrix}-\boldsymbol{G}_d\boldsymbol{W}_{d\mathrm{mad}}-\omega_eL_q\boldsymbol{W}_{q\mathrm{mad}}\\ \omega_eL_d\boldsymbol{W}_{d\mathrm{mad}}-\boldsymbol{G}_q\boldsymbol{W}_{q\mathrm{mad}}\end{bmatrix}\\&\quad+\begin{bmatrix}-U_{q\mathrm{ref},0}\\ U_{d\mathrm{ref},0}\end{bmatrix}\boldsymbol{G}_{\mathrm{mad}}.\end{aligned} \tag{32}$$

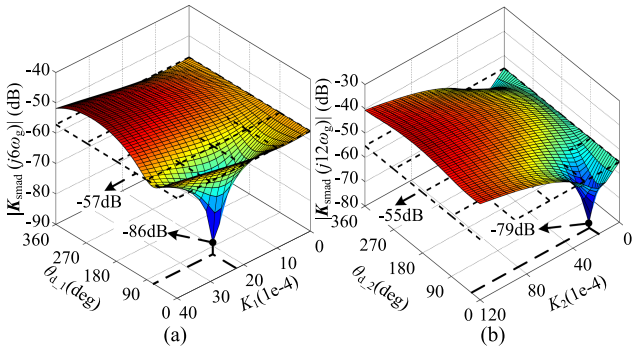

Fig. 8. Magnitudes of $\boldsymbol{K}_{\mathrm{smad}}(s)$ with different amplitudes and phases of correction components. (a) At the frequency of $6\omega_g$. (b) At the frequency of $12\omega_g$.

From (19), (31), and (32), $\boldsymbol{G}_{\mathrm{smad}}(s)$ can be rewritten as

$$\begin{aligned}\boldsymbol{G}_{\mathrm{smad}}=\boldsymbol{G}_{\mathrm{s}}-\frac{\boldsymbol{G}_{\mathrm{mad}}}{U_{\mathrm{sref},0}}\Bigg[&\frac{U_{q\mathrm{ref},0}\left(\omega_eL_dU_{q\mathrm{ref},0}-U_{d\mathrm{ref},0}\boldsymbol{G}_d\right)}{R_s+L_ds+\boldsymbol{G}_d}\\&+\frac{U_{d\mathrm{ref},0}\left(\omega_eL_qU_{d\mathrm{ref},0}+U_{q\mathrm{ref},0}\boldsymbol{G}_q\right)}{R_s+L_qs+\boldsymbol{G}_q}\Bigg]\end{aligned} \tag{33}$$

where $\boldsymbol{G}_{\mathrm{smad}}(s)$ is the transfer function between $\Delta|\boldsymbol{u}_{\mathrm{sref}}|$ and Δu_{dc} with the proposed strategy.

According to (33), the relationship between the modulation index and the dc-link voltage can be derived as $\boldsymbol{K}_{\mathrm{smad}}(s)$

$$\boldsymbol{K}_{\mathrm{smad}}(s)=\frac{\Delta m}{\Delta u_{\mathrm{dc}}}=\frac{\sqrt{3}\left(U_{\mathrm{dc},0}\boldsymbol{G}_{\mathrm{smad}}-U_{\mathrm{sref},0}e^{-0.5sT_s}\right)}{U_{\mathrm{dc},0}^2}. \tag{34}$$

According to (33) and (34), the amplitude and phase of $\boldsymbol{M}_{d\_1}(s)$ and $\boldsymbol{M}_{d\_2}(s)$ can be theoretically designed with the guidance of $\boldsymbol{K}_{\mathrm{smad}}(s)$ at the frequencies of $6\omega_g$ and $12\omega_g$. The magnitude of $\boldsymbol{K}_{\mathrm{smad}}(j6\omega_g)$ with different amplitudes and phases of $\boldsymbol{M}_{d\_1}(s)$ is shown in Fig. 8(a). $|\boldsymbol{K}_{\mathrm{smad}}(j6\omega_g)|$ is reduced from -57 to -86 dB when K_1 and θ_{d_1} are set as 2.2e-3 and 72°, respectively. The magnitudes of $\boldsymbol{K}_{\mathrm{smad}}(j12\omega_g)$ with different amplitudes and phases of $\boldsymbol{M}_{d\_2}(s)$ are demonstrated in Fig. 8(b). $|\boldsymbol{K}_{\mathrm{smad}}(j12\omega_g)|$ is decreased from -55 to -79 dB when K_2 and θ_{d_2} are set as 1.8e-3 and 30°, respectively, which illustrates that the control method can reduce the harmonic of modulation index at the frequencies of $6\omega_g$ and $12\omega_g$, effectively.

Substituting the designed parameters of correction components into (34), the Bode diagrams of $\boldsymbol{K}_{\mathrm{smad}}(s)$ before and after applying the proposed method are shown in Fig. 9. It can be seen that the magnitudes of $\boldsymbol{K}_{\mathrm{smad}}(s)$ at the frequencies of $6\omega_g$ and $12\omega_g$ are reduced to -89 and -85 dB, which ameliorates the linear modulation margin.

The harmonic at the frequency of $6\omega_g$ in the dc-link voltage leads to the dominate fluctuation in the modulation index. Hence, the linear modulation margin M_{mar} can be expressed as

$$\begin{aligned}M_{\mathrm{mar}}&=1-\frac{\sqrt{3}U_{\mathrm{sref},0}}{U_{\mathrm{dc},0}}-U_{\mathrm{dc},1}\cdot\left|\boldsymbol{K}_{\mathrm{smad}}(j6\omega_g)\right|\\&=1-M_0-U_{\mathrm{dc},1}\cdot\left|\boldsymbol{K}_{\mathrm{smad}}(j6\omega_g)\right|.\end{aligned} \tag{35}$$

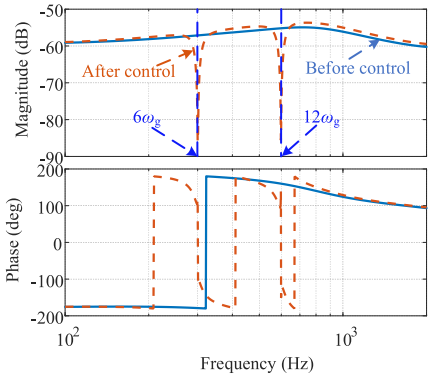

Fig. 9. Bode diagrams of $\boldsymbol{K}_{\mathrm{smad}}(s)$ before and after applying the method.

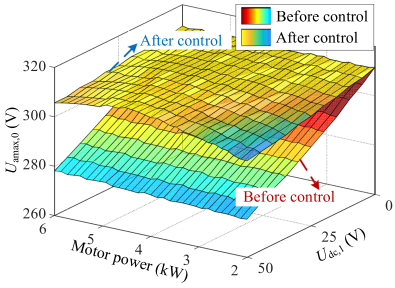

Fig. 10. Maximum amplitude of the fundamental motor voltage under different powers and harmonic of DC-link voltage.

From (35), the average value of the maximum modulation index $M_{0,\max}$ in the linearly modulated system is

$$M_{0,\max} = 1 - U_{\mathrm{dc},1} \cdot \left| \boldsymbol{K}_{\mathrm{smad}}\left(j6\omega_g\right) \right|. \tag{36}$$

The influence of the control method on the utilization of dc-link voltage should be analyzed. From (36) and (A5), the maximum amplitude of the fundamental motor voltage at the linear modulation can be expressed as

$$U_{a\max,0} = \sqrt{U_{\mathrm{dc},0}^2 [1 - U_{\mathrm{dc},1} \left| \boldsymbol{K}_{\mathrm{smad}}\left(j6\omega_g\right) \right|]^2 + \left(U_6 + U_{12}\right)^2} \tag{37}$$

where $U_{a\max,0}$ is the maximum amplitude of the fundamental motor voltage at the linear modulation, U_6 and U_{12} are the amplitude increments introduced by the regulated angle at the frequencies of $6\omega_g$ and $12\omega_g$, respectively, which are shown in (A5).

According to (37), the maximum amplitude of the fundamental voltage under different motor frequencies and harmonic of dc-link voltage are shown in Fig. 10. Due to the fluctuation of dc-link voltage, the maximum amplitude of the motor phase voltage without control is reduced to 270 V as the harmonic amplitude of dc-link voltage increases to 50 V. The linear modulation expansion method can increase the maximum amplitude to over 300 V, which can maintain the control performance under the variation of motor power.

From [35] and [36], the overmodulation and the nonlinear factors of the inverter operation will introduce the harmonics at the frequencies of $(2k+1)\omega_e$ in the reference voltage. Due to the fluctuation of the dc-link voltage, the motor currents and voltages exist additional harmonics at the frequencies of $6k\omega_e$, $6k\omega_g$, and $6(k_2\omega_g \pm k_1\omega_e)$, which can be expressed as

$$\begin{aligned} i_{d,q} &= \sum_{k=1}^{n} I_{d,qg,k} \sin(6k\omega_{\mathrm{g}} t + \varphi_{d,qgk}) \\ &+ I_{d,qe,k} \sin(6k\omega_e t + \varphi_{d,qek}) \\ &+ \sum_{k_1=1}^{\infty} \sum_{k_2=1}^{\infty} \{ I_{d,q+,(k1,k2)} \sin\left[6\left(k_2\omega_g + k_1\omega_e\right)t + \varphi_{d,q+,(k1,k2)}\right] \\ &+ I_{d,q-,(k1,k2)} \sin\left[6\left(k_2\omega_g - k_1\omega_e\right)t + \varphi_{d,q-,(k1,k2)}\right] \} + I_{d,q,0} \end{aligned} \tag{38}$$

where $I_{d,0}$ and $I_{q,0}$ are the average values of the motor currents in dq-axes, $I_{d,qg,k}$, $\varphi_{d,qgk}$, $I_{d,qe,k}$, $\varphi_{d,qek}$, $I_{d,q+,(k1,k2)}$, $\varphi_{d,q+,(k1,k2)}$, $I_{d,q-,(k1,k2)}$, and $\varphi_{d,q-,(k1,k2)}$ are the amplitudes and phases of the dominated harmonics in dq-axis motor currents, respectively.

The harmonics related to the motor speed are generated by the inverter side. According to the power balance of the inverter, the input impedance of the inverter can be denoted as (39) after applying the proposed strategy

$$\begin{aligned} \boldsymbol{Z}_{m\mathrm{mad}} = \frac{\Delta u_{\mathrm{dc}}}{\Delta i_{\mathrm{inv}}} = \Bigg[& \frac{3\boldsymbol{W}_{d\mathrm{mad}}(U_{d,0} + \omega_e L_d I_{q,0} + L_d I_{d,0} s + I_{d,0} R_s)}{2U_{\mathrm{dc},0}} \\ & + \frac{3\boldsymbol{W}_{q\mathrm{mad}}(U_{q,0} - \omega_e L_q I_{d,0} + L_q I_{q,0} s + I_{\mathrm{q},0} R_{\mathrm{s}})}{2U_{\mathrm{dc},0}} - \frac{I_{\mathrm{inv},0}}{U_{\mathrm{dc},0}} \Bigg]^{-1} \end{aligned} \tag{39}$$

where $I_{\mathrm{inv},0}$, $U_{d,0}$, and $U_{q,0}$ are the average values of the inverter current and the motor voltages in dq-axes, respectively, Δi_{inv} is the small variation of the inverter current. $\boldsymbol{Z}_{m\mathrm{mad}}(s)$ is the transfer function of the input impedance.

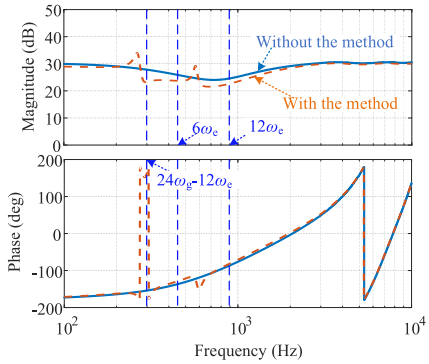

Fig. 11. Bode diagrams of $\boldsymbol{Z}_{m\mathrm{mad}}(s)$ before and after applying the method.

The straight line in Fig. 11 shows the Bode diagram of $\boldsymbol{Z}_{m\mathrm{mad}}(s)$ without the proposed method. The magnitude is over 20 dB at the frequencies of $6k\omega_e$ and $6(k_2\omega_g \pm k_1\omega_e)$, which means the dc-link voltage exists other harmonic components caused by the inverter operation.

As the operation frequency satisfies the condition in (40), the frequencies of the harmonics caused by the inverter operation are equal to $6k\omega_g$, which affects the amplitudes and phases of the 6th-order components caused by rectifier side

$$\omega_e = k_2\omega_g / k_1. \tag{40}$$

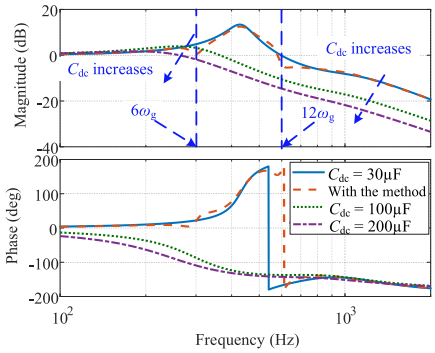

Fig. 12. Bode diagrams of $\boldsymbol{G}_{u\mathrm{mad}}(s)$ under different values of C_{dc}.

The dash line in Fig. 11 shows the Bode diagram when applying the proposed method, and the inverter generates the harmonics at the frequency of $6k\omega_g$ in the dc-link voltage. As can be seen, the magnitudes at the frequencies of $6\omega_e$, and $12\omega_e$ can be reduced by 3.5 dB. Meanwhile, the magnitude at the frequency of $6\omega_g$ can be decreased from 28 to 23 dB, which illustrates that the linear modulation region expansion strategy can reduce the dc-link harmonics caused by the inverter operation.

In order to further analyze the dc-link voltage ripples caused by the rectifier side, the transfer function of the voltage relationship $\boldsymbol{G}_{u\mathrm{mad}}(s)$ can be presented as

$$\boldsymbol{G}_{u\mathrm{mad}}(s)=\frac{\Delta u_{\mathrm{dc}}(s)}{\Delta u_{\mathrm{grec}}(s)}=\frac{1}{1+(L_g s+R_g)\left[\boldsymbol{Z}_{m\mathrm{mad}}^{-1}+C_{\mathrm{dc}}s\right]} \tag{41}$$

where Δu_{grec} is the small signal variation of the rectifier output voltage, L_g and C_{dc} are the line inductance and the dc-link capacitance, respectively.

The Bode diagrams of $\boldsymbol{G}_{u\mathrm{mad}}(s)$ with different values of dc-link capacitance are shown in Fig. 12. The magnitudes at the frequencies of $6k\omega_g$ decrease as the capacitance increases, which means the magnitudes of the dc-link ripples are reduced as well. The dash line shows the Bode diagram with the proposed method, and the magnitudes at the frequencies of $6\omega_g$ and $12\omega_g$ can be reduced by 4 dB. That means the proposed strategy can extend the linear modulation region without increasing the dc-link voltage ripples.

IV. Experimental Results

The performance of the proposed method is verified on a 5.5 kW experimental platform of the drive system equipped with slim film capacitor shown in Fig. 13. The film capacitor and filter inductance are selected as 30 μF and 2.5 mH, respectively. The ac input of the inverter is 380-Vrms (50 Hz). The motor parameters of L_d, L_q, R_s are 7.5 mH, 17.2 mH, and 0.265 Ω, respectively. The whole control algorithm is realized by the digital controller TMS320F28075. The switching cycle T_s is 1.25e-4 s. The test PMSM is connected with a load PMSM using a shaft. The load PMSM is working in the regenerating mode, and the regenerated power is consumed in a resistor.

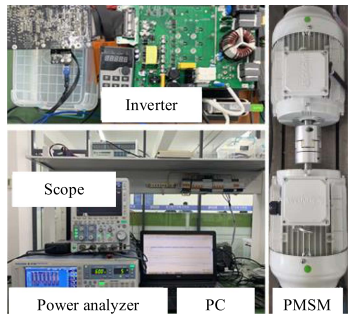

Fig. 13. Experimental platform of the PMSM drive system equipped with slim film capacitors.

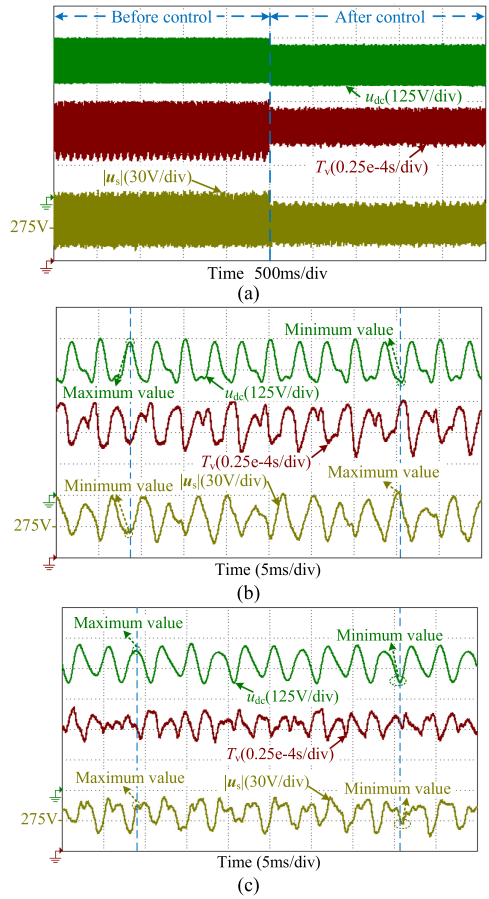

Fig. 14. Experimental results at the operation frequency of 74 Hz. (a) Enable the proposed strategy. (b) Zoomed view with the proposed strategy. (c) Zoomed view without the proposed strategy.

Fig. 14(a) shows the experimental results at the operation frequency of 74 Hz. The waveforms from the top to the bottom are the dc-link voltage, the total dwell time of voltage vector, and the amplitude of voltage vector, respectively. The total dwell time before control reaches 1.25e-4 s, meaning that the system operates in the overmodulation region. The control strategy leads to the total dwell time less than 1.25e-4 s, which means the SVPWM is operating in linear modulation. Meanwhile, the peak-to-peak value of the voltage vector amplitude is decreased from 64.2 to 40.9 V, and the voltage distortion can be suppressed.

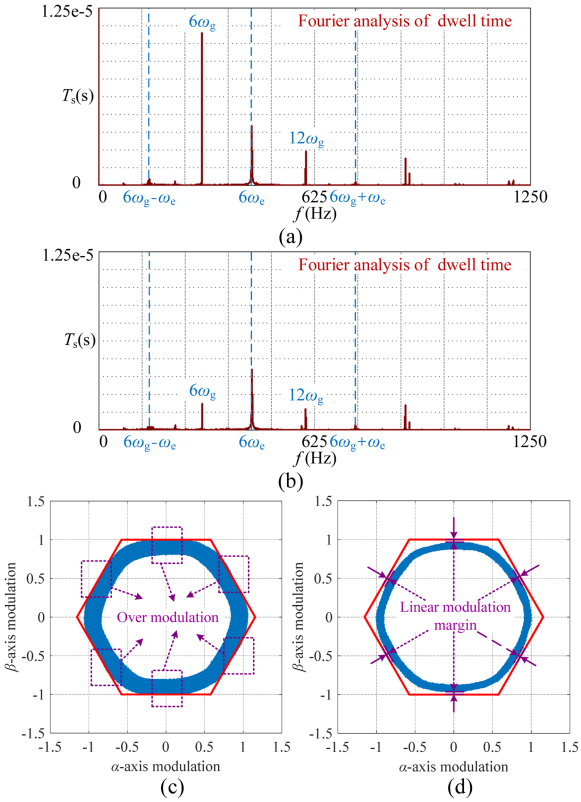

Fig. 15. Experimental results of dwell time and modulation index at the motor frequency of 74 Hz. (a) Fourier analysis of dwell time without the method. (b) Fourier analysis of dwell time with the method. (c) Modulation index in $\alpha\beta$-axes without the method. (d) Modulation index in $\alpha\beta$-axes with the method.

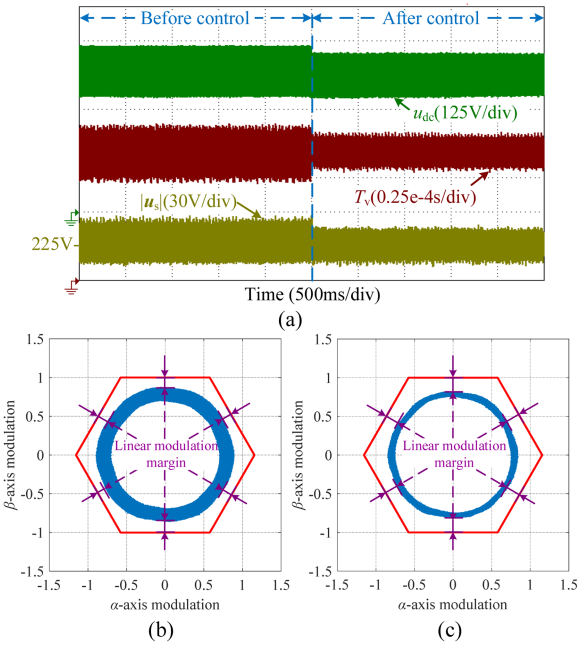

Fig. 16. Experimental results at the operation frequency of 62 Hz. (a) Enable the proposed strategy. (b) Modulation index in $\alpha\beta$-axes without the method. (c) Modulation index in $\alpha\beta$-axes with the method.

Fig. 14(b) and (c) are the zoomed view of experimental results with and without the proposed strategy. The fluctuation frequency of the voltage vector amplitude is the same as that of the dc-link voltage. The maximum value of voltage vector amplitude is synchronous with the minimum value of dc-link voltage. The phase difference between the two fluctuations is 180°, which leads to the deterioration of modulation index. The fundamental frequency of total dwell time is six times of the motor frequency as analyzed in Section II. The maximum value of the voltage vector amplitude corresponds to that of the dc-link voltage, which can suppress the amplitude of modulation fluctuation from 0.50e-4 s to 0.30e-4 s effectively.

Fig. 15(a) and (b) are the Fourier analysis of total dwell time with and without the proposed strategy at the motor frequency of 74 Hz. As shown in Fig. 15(a), the dwell time of basic voltage vectors contains the fundamental component at the frequency of 444 Hz and other harmonics at the frequencies of 300 and 600 Hz. The frequencies of main harmonics are the same as those in the dc-link voltage. The linear modulation expansion method can reduce the harmonics at the frequency of 300 and 600 Hz from 1.08e-5 s and 0.24e-5 s to 0.18e-5 s and 0.14e-5 s, respectively. The modulation index in $\alpha\beta$-axes with and without the strategy are shown in Fig. 15(c) and (d). Without the proposed method, the amplitude of the modulation index will locate in the boundary of the hexagon, which means the system enters the overmodulation region, as shown in Fig. 15(c). After applying the proposed method, the fluctuation of modulation index falls from 0.22 to 0.10. The amplitude of the modulation index will not reach the boundary of the hexagon at the same operation condition of the motor, which means the linear modulation region is enlarged.

For the aim of proving the control performance in the linear modulation region, experimental results at operation frequency of 62 Hz are shown in Fig. 16. Before applying the proposed method, the maximum value of the total dwell time is less than 1.25e-4 s, which means that the system is linear modulated. The expansion strategy can decrease the maximum dwell time from 1.14e-4 s to 1.02e-4 s, which increases the linear modulation margin. As can be seen in Fig. 16(a), the peak-to-peak value of the voltage vector amplitude is restrained from 44.8 to 27 V. Fig. 16(b) and (c) show the $\alpha\beta$-axis components of modulation index. The modulation index fluctuation is suppressed from 0.18 to 0.07, and the distance between the boundary hexagon and the amplitude of modulation index are increased after applying the method, which results in the improvement of linear modulation margin.

In order to evaluate the performance at the time point of enabling the proposed strategy, the waveforms of the dc-link voltage, the voltage vector amplitude, the motor position and the motor speed are shown in Fig. 17. It is seen that the peak-to-peak value of the motor speed ripple falls from 56 to 24 r/min, and there is no overshoot during the enabling process. As a result, due to the expansion of the linear modulation region, the fluctuation of the dc-link voltage and the speed can be reduced effectively.

Fig. 18 shows the experimental results of attainable motor frequency in linear modulation. It can be known from Fig. 18(a) that the attainable motor frequency is 71 Hz without the method,

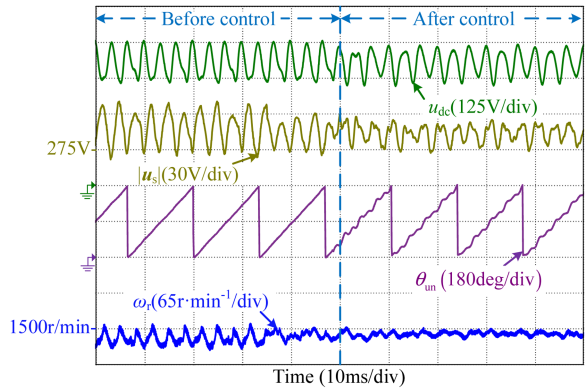

Fig. 17. Experimental results at the time point of enabling the proposed method.

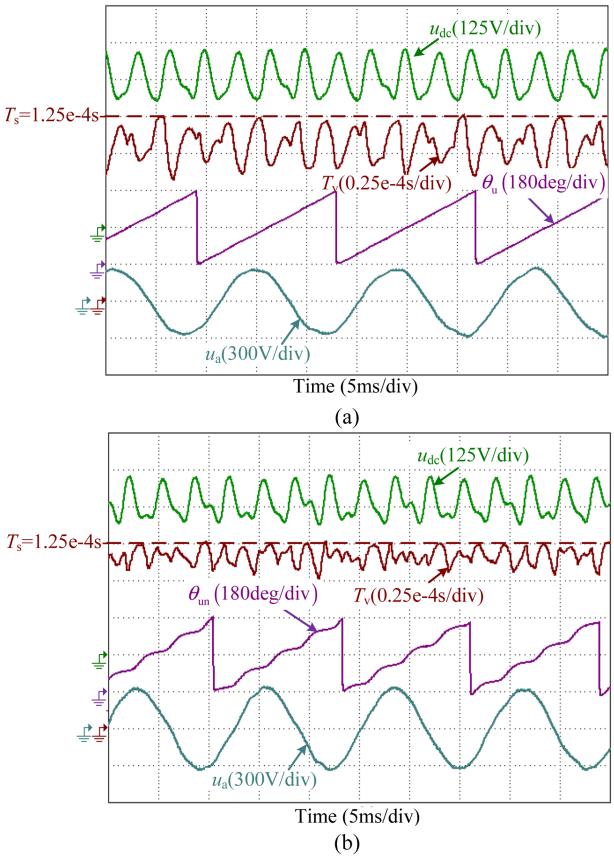

Fig. 18. Experimental results of attenable motor frequency. (a) Without the control method (71 Hz). (b) With the control method (80 Hz).

which is operating when the linear modulation margin is close to 0 with the serious distortion of dwell time. Fig. 18(b) show the results after applying the proposed method, the modulation index ripples are suppressed while the attainable frequency reaches 80 Hz when the linear modulation margin is close to 0. Consequently, by applying the proposed method, the attainable motor speed can be increased by 12.7%. The amplitude of a-axis voltage increases from 265 to 302 V, which means the utilization of dc-link voltage can be improved by 13.2%.

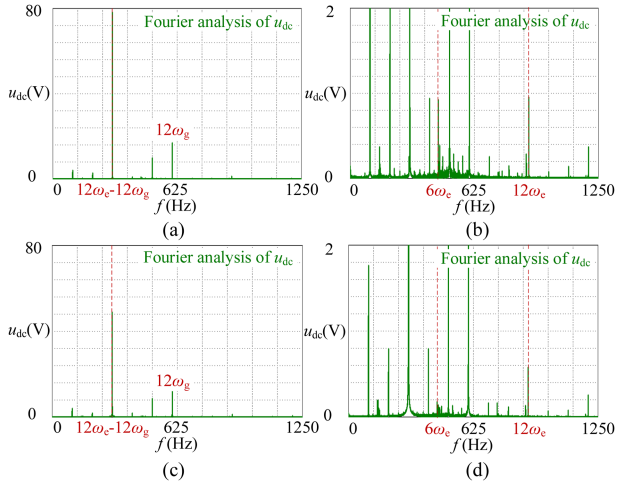

Fig. 19. Fourier analysis of DC-link voltage at the operation frequency of 75 Hz. (a) Without the method. (b) Zoomed view of (a). (c) With the method. (d) Zoomed view of (c).

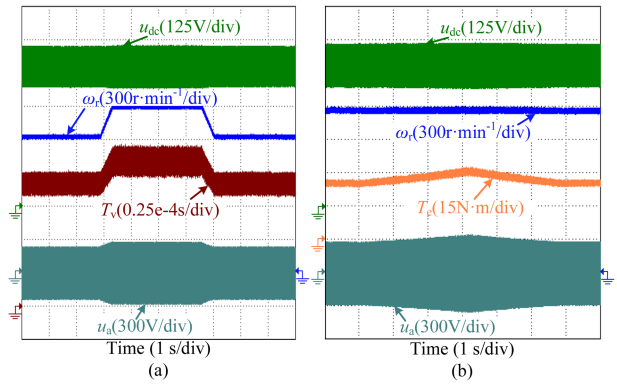

Fig. 20. Dynamic experimental waveforms of the proposed method. (a) Speed dynamic process. (b) Load torque dynamic process.

Fig. 19(a)–(d) are the Fourier analysis of dc-link voltage with and without the proposed strategy at the operation frequency of 75 Hz. The dc-link voltage contains the components from the rectifier at the frequencies of 300 and 600 Hz, and other harmonics from the inverter at the frequencies of 450 and 900 Hz. The linear modulation expansion method can suppress the harmonics at the frequencies of 450 and 900 Hz from 0.96 and 0.98 V to 0.01 and 0.58 V, respectively. Meanwhile, the amplitude of the harmonics at the frequency of 300 Hz is also reduced from 78.2 to 48.5 V.

The experimental waveforms of variable speed operation are shown in Fig. 20(a) when the motor speed varies from 1240 r/min to 1480 r/min and back to 1240 r/min. It can be seen from the region of rising that the amplitude of dc-link voltage fluctuation increases from 74 to 81 V, which is on the contrary in the region of declining.

Fig. 20(b) shows the experimental waveforms when the load torque varies between 25 and 32 N·m. The stability of motor speed is not be deteriorated, and there is no drop of dc-link voltage during the torque and speed variation. Hence the proposed method maintains stable control performance in the applications

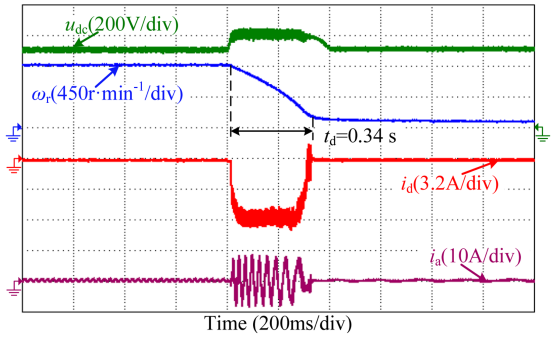

Fig. 21. Experimental results of the braking process when the speed decreases from 45 to 5 Hz.

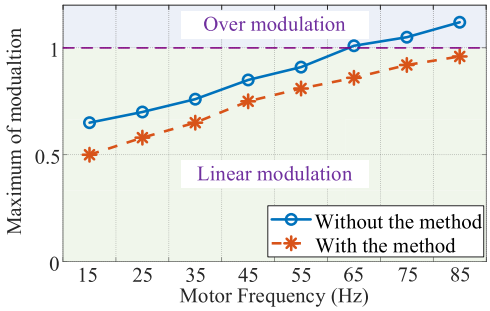

Fig. 22. Maximum value of modulation index under different motor frequencies.

with more tolerance of dynamic performance, and torque and speed ripple.

In order to enhance the performance of the braking process, the dual antiovervoltage method shown in [37] is applied with the proposed strategy. Fig. 21 shows the experimental results when the speed decreases from 45 to 5 Hz. The dc-link voltage is controlled around 640 V during deceleration process. Consequently, the speed deceleration time can be reduced to 0.34 s from 45 to 5 Hz, which means the dynamic performance of the regeneration operation has been regulated effectively.

Fig. 22 shows the maximum value of the modulation index under the condition of different operation frequencies. As can be seen, SVPWM will enter the overmodulation region when the motor frequency is 65 Hz without applying the proposed method. The maximum value of the modulation index can be reduced by over 0.1 with the proposed method in whole frequency range, and the frequency boundary of the linear modulation is improved from 65 to 85 Hz.

Fig. 23(a) shows the maximum value of the of attainable motor frequency under different values of load torque. As can be seen, the maximum motor frequency will reduce to 65 Hz when the load torque increases to 36 N·m without applying the proposed method. The maximum value of attainable motor frequency can be improved by over 5 Hz with the proposed method in the torque range between 22 and 36 N·m.

Fig. 23(b) shows the copper loss under different values of load torque. The power loss of the stator resistance will become over 200 W when the load torque increases to 32 N·m before applying the proposed method. The copper loss can be reduced by over 13 W with the proposed method applied.

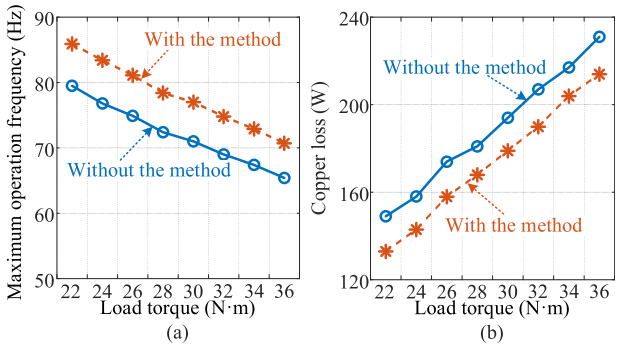

Fig. 23. Experimental results of maximum operation frequency and copper loss under different load torques. (a) Maximum value of attainable operation frequency. (b) Copper loss of the stator resistance.

V. Conclusion

In this article, a voltage vector angle regulation based linear modulation expansion method is investigated. The dc-link voltage ripple introduced additional harmonics to the modulation index, which causes the additional fluctuation of motor voltage and the reduction of voltage utilization. The influence of the dc-link fluctuation to the amplitude of voltage vector reference was analyzed mathematically, and the phase differences between the voltages causes the harmonics of modulation index. The harmonics of dc-link voltage was applied to regulate the angle of voltage space vector through the correction components. According to the small-signal model of the drive system, the harmonics of modulation index can be suppressed and the dc-link utilization can be improved through applying the control method. Experimental results verified that the amplitudes of the modulation index harmonics caused by dc-link fluctuation was reduced by 80%, and the dc-link utilization was increased by 13.2%. The proposed method can improve the operation range and the margin of motor voltage output in the linear modulation region, which can be also applied in the configurations with single-phase bridge rectifier system feeding different types of motor.

Appendix

From (21) and (25), the frequency characteristics of $\boldsymbol{M}_{d\_1}(s)$ and $\boldsymbol{M}_{d\_2}(s)$ at the frequencies of $6\omega_g$ and $12\omega_g$ are expressed as

$$\begin{cases} \boldsymbol{M}_{d\_1}(j6\omega_g) = K_1(\cos\theta_{d\_1} + j\sin\theta_{d\_1}) \\ \boldsymbol{M}_{d\_2}(j12\omega_g) = K_2(\cos\theta_{d\_2} + j\sin\theta_{d\_2}) \end{cases} \tag{A1}$$

where

$$\begin{cases} K_1 = \frac{A_6}{U_{\mathrm{dc},1}}, \theta_{d\_1} = \varphi_{u6} - \varphi_1 - 3\omega_g T_s \\ K_2 = \frac{A_{12}}{U_{\mathrm{dc},2}}, \theta_{d\_2} = \varphi_{u12} - \varphi_2 - 6\omega_g T_s \end{cases}. \tag{A2}$$

The a-axis motor voltage can be expressed as

$$\begin{aligned} u_a &= mu_{\mathrm{dc}}\sin(\omega_e t + \theta_u + \Delta\theta_u) \\ &\approx mu_{\mathrm{dc}}[\sin(\omega_e t + \theta_u) + \Delta\theta_u\cos(\omega_e t + \theta_u)] \end{aligned} \tag{A3}$$

where u_a is the a-axis motor voltage.

Substituting (1) and (4) into (A3), the a-axis motor voltage contains the harmonics at the frequencies of ω_e, ($6k\omega_g$-ω_e)

and $(6k\omega_g+\omega_e)$. The fundamental component of a-axis motor voltage can be expressed as

$$u_{a,0} = M_0 U_{\mathrm{dc},0} \sin(\omega_e t + \theta_u) + (U_6 + U_{12}) \cos(\omega_e t + \theta_u) \tag{A4}$$

where $u_{a,0}$ is the fundamental component of a-axis motor voltage. U_6 and U_{12} can be presented as

$$\begin{cases} U_6 = 0.5A_6 \left[M_0 U_{\mathrm{dc},1} \cos(\varphi_1 - \varphi_{u6}) \right. \\ \qquad \left. + M_1 U_{\mathrm{dc},0} \cos(\varphi_{g1} - \varphi_{\mathrm{u6}}) \right] \\ U_{12} = 0.5A_{12} \left[M_0 U_{\mathrm{dc},2} \cos(\varphi_2 - \varphi_{u12}) \right. \\ \qquad \left. + M_2 U_{\mathrm{dc},0} \cos(\varphi_{g2} - \varphi_{u12}) \right] \end{cases}. \tag{A5}$$

REFERENCES

[1] G. Wu, S. Huang, Q. Wu, F. Rong, C. Zhang, and W. Liao, "Robust predictive torque control of N*3-phase PMSM for high-power traction application," *IEEE Trans. Power Electron.*, vol. 35, no. 10, pp. 10799–10809, Oct. 2020.

[2] S. Zhao, X. Huang, Y. Fang, and H. Zhang, "DC-link-fluctuation-resistant predictive torque control for railway traction permanent magnet synchronous motor in the six-step operation," *IEEE Trans. Power Electron.*, vol. 35, no. 10, pp. 10982–10993, Oct. 2020.

[3] K. Yu and Z. Wang, "Improved deadbeat predictive current control of dual three-phase variable-flux PMSM drives with composite disturbance observer," *IEEE Trans. Power Electron.*, vol. 37, no. 7, pp. 8310–8321, Jul. 2022.

[4] X. Li et al., "A novel voltage-boosting modulation strategy to reduce DC-link capacitance for brushless DC motor drives," *IEEE Trans. Power Electron.*, vol. 37, no. 12, pp. 15397–15410, Dec. 2022.

[5] N. Zhao, R. Gao, G. Wang, D. Ding, G. Zhang, and D. Xu, "Online estimation method of DC-link capacitors for reduced DC-link capacitance IPMSM drives," *IEEE Trans. Power Electron.*, vol. 36, no. 11, pp. 12196–12201, Nov. 2021.

[6] J. Huo, N. Zhao, G. Wang, G. Zhang, L. Zhu, and D. Xu, "An active damping control method for reduced DC-link capacitance PMSM drives with low line inductance," *IEEE Trans. Power Electron.*, vol. 37, no. 12, pp. 14328–14342, Dec. 2022.

[7] B. S. Umesh and K. Sivakumar, "Pole-phase modulated multiphase induction motor drive with reduced torque ripple and improved DC link utilization," *IEEE Trans. Power Electron.*, vol. 32, no. 10, pp. 7862–7269, Oct. 2017.

[8] H. Wang, H. S. Chung, and W. Liu, "Use of a series voltage compensator for reduction of the DC-link capacitance in a capacitor-supported system," *IEEE Trans. Power Electron.*, vol. 29, no. 3, pp. 1163–1175, Mar. 2014.

[9] Y. Bai et al., "An adaptive-frequency harmonic suppression strategy based on vector reconstruction for current measurement error of PMSM drives," *IEEE Trans. Power Electron.*, vol. 38, no. 1, pp. 34–40, Jan. 2023.

[10] L. Zheng, R. P. Kandula, and D. Divan, "Robust predictive control for modular solid-state transformer with reduced DC-link and parameter mismatch," *IEEE Trans. Power Electron.*, vol. 36, no. 12, pp. 14295–14311, Dec. 2021.

[11] D. Ding, G. Wang, N. Zhao, G. Zhang, and D. Xu, "Enhanced flux-weakening control method for reduced dc-link capacitance IPMSM drives," *IEEE Trans. Power Electron.*, vol. 34, no. 8, pp. 7788–7799, Aug. 2019.

[12] G. Wang, H. Hu, D. Ding, N. Zhao, Y. Zou, and D. Xu, "Overmodulation strategy for electrolytic capacitorless PMSM drives: Voltage distortion analysis and boundary optimization," *IEEE Trans. Power Electron.*, vol. 35, no. 9, pp. 9574–9585, Sep. 2020.

[13] C. Yin, W. Ding, L. Ming, and P. C. Loh, "Single-stage active split-source inverter with high DC-link voltage utilization," *IEEE Trans. Power Electron.*, vol. 36, no. 6, pp. 6699–6711, Jun. 2021.

[14] H. Heydari-Doostabad and S. H. Hosseini, "Pseudo DC-link EV home charger with a high semiconductor device utilization factor," *IEEE Trans. Ind. Electron.*, vol. 69, no. 3, pp. 2459–2469, Mar. 2022.

[15] A. G. Yepes and J. Doval-Gandoy, "Simple carrier-based PWM for prolonged high DC-link utilization for symmetrical and asymmetrical n-phase AC drives," *IEEE Trans. Power Electron.*, vol. 36, no. 8, pp. 8696–8712, Aug. 2021.

[16] P. Strajnikov and A. Kuperman, "DC-link capacitance reduction in PFC rectifiers employing PI+notch voltage controllers," *IEEE Trans. Power Electron.*, vol. 38, no. 1, pp. 977–986, Jan. 2023.

[17] M. K. Pinjala and R. Bhimasingu, "Improving the DC-link utilization of nine-switch boost inverter suitable for six-phase induction motor," *IEEE Trans. Transp. Electrific.*, vol. 6, no. 3, pp. 1177–1187, Sep. 2020.

[18] S. A. M. Saleh et al., "Solid-state transformers for distribution systems–part I: Technology and construction," *IEEE Trans. Ind. Appl.*, vol. 55, no. 5, pp. 4524–4535, Sep./Oct. 2019.

[19] R. Goel, T. T. Davis, and A. Dey, "Thirteen-level multilevel inverter structure having single DC source and reduced device count," *IEEE Trans. Ind. Appl.*, vol. 58, no. 4, pp. 4932–4942, Jul./Aug. 2022.

[20] B. P. Reddy, M. Rao A, M. Sahoo, and S. Keerthipati, "A fault-tolerant multilevel inverter for improving the performance of a pole–phase modulated nine-phase induction motor drive," *IEEE Trans. Ind. Electron.*, vol. 65, no. 2, pp. 1107–1116, Feb. 2018.

[21] A. G. Yepes, J. Doval-Gandoy, and H. A. Toliyat, "Improvement in DC-link utilization with reduced current and torque deterioration for five-phase drives by combination of circulating-current filters and simple carrier-based PWM based on closed-form expressions," *IEEE Trans. Ind. Electron.*, vol. 68, no. 2, pp. 960–971, Feb. 2021.

[22] B. Yu, W. Song, and Y. Guo, "A finite control set model predictive control for five-phase PMSMs with improved DC-link utilization," *IEEE Trans. Power Electron.*, vol. 37, no. 3, pp. 3297–3307, Mar. 2022.

[23] V. Repecho, A. Sierra-González, E. Ibarra, D. Biel, and A. Arias, "Enhanced DC-link voltage utilization for sliding-mode-controlled PMSM drives," *IEEE Trans. Emerg. Sel. Topics Power Electron.*, vol. 9, no. 3, pp. 2850–2857, Jun. 2021.

[24] S. A. Khajehoddin, M. Karimi-Ghartemani, and M. Ebrahimi, "Grid-supporting inverters with improved dynamics," *IEEE Trans. Ind. Electron.*, vol. 66, no. 5, pp. 3655–3667, May 2019.

[25] B. Ge et al., "Direct instantaneous ripple power predictive control for active ripple decoupling of single-phase inverter," *IEEE Trans. Ind. Electron.*, vol. 65, no. 4, pp. 3165–3175, Apr. 2018.

[26] S. S. Lee, Y. P. Siwakoti, R. Barzegarkhoo, and K.-B. Lee, "Switched-Capacitor-based five-level T-type inverter (SC-5TI) with soft-charging and enhanced DC-link voltage utilization," *IEEE Trans. Power Electron.*, vol. 36, no. 12, pp. 13958–13967, Dec. 2021.

[27] X. Li et al., "A novel voltage-boosting modulation strategy to reduce DC-link capacitance for brushless DC motor drives," *IEEE Trans. Power Electron.*, vol. 37, no. 12, pp. 15397–15410, Dec. 2022.

[28] G. Wang, M. Valla, and J. Solsona, "Position sensorless permanent magnet synchronous machine drives—A review," *IEEE Trans. Ind. Electron.*, vol. 67, no. 7, pp. 5830–5842, Jul. 2020.

[29] G. Wang, R. Yang, and D. Xu, "DSP-based control of sensorless IPMSM drives for wide-speed range operation," *IEEE Trans. Ind. Electron.*, vol. 60, no. 2, pp. 720–727, Feb. 2013.

[30] N. Zhao, G. Wang, D. Ding, G. Zhang, and D. Xu, "Impedance based stabilization control method for reduced DC-link capacitance IPMSM drives," *IEEE Trans. Power Electron.*, vol. 34, no. 10, pp. 9879–9890, Oct. 2019.

[31] D. Ding et al., "Impedance reshaping for inherent harmonics in PMSM drives with small DC-link capacitor," *IEEE Trans. Power Electron.*, vol. 37, no. 12, pp. 14265–14279, Dec. 2022.

[32] X. Huang, X. Ruan, J. Fang, and S. Kan, "A virtual impedance based control scheme for modular electrolytic capacitor-less second harmonic current compensator," *IEEE Trans. Ind. Electron.*, vol. 68, no. 1, pp. 198–209, Jan. 2021.

[33] C. Wang and Z. Q. Zhu, "Fuzzy logic speed control of permanent magnet synchronous machine and feedback voltage ripple reduction in flux-weakening operation region," *IEEE Trans. Ind. Appl.*, vol. 56, no. 2, pp. 1505–1517, Mar./Apr. 2020.

[34] A. Z. Albanna and C. J. Hatziadoniu, "Harmonic modeling of hysteresis inverters in frequency domain," *IEEE Trans. Power Electron.*, vol. 25, no. 5, pp. 1110–1114, May 2010.

[35] X. Zhang, B. Wang, Y. Yu, J. Zhang, and D. Xu, "Overmodulation index optimization method for torque quality improvement in induction motor field-weakening control," *IEEE Trans. Ind. Electron.*, vol. 68, no. 12, pp. 11954–11967, Dec. 2021.

[36] X. Wu et al., "Enhanced position sensorless control using bilinear recursive least squares adaptive filter for interior permanent magnet synchronous motor," *IEEE Trans. Power Electron.*, vol. 35, no. 1, pp. 681–698, Jan. 2020.

[37] D. Ding, G. Zhang, G. Wang, and D. Xu, "Dual antiovervoltage control scheme for electrolytic capacitorless IPMSM drives with coefficient autoregulation," *IEEE Trans. Power Electron.*, vol. 35, no. 3, pp. 2895–2907, Dec. 2022.

Runfeng Gao received the B.S. and the M.S. degrees in electrical engineering from Harbin Institute of technology, China in 2020 and 2022, respectively. He is currently working toward the Ph.D. degree in power electronics and electrical drives with Harbin institute of technology, Harbin, China

His current research interests include advanced control strategies for PMSM system and electrolytic capacitor-less drives.

Dawei Ding (Member, IEEE) received the B.S and M.S degrees in electrical engineering from Hefei University of Technology, Hefei, China, in 2014 and 2017, respectively, and the Ph.D. degree in electrical engineering from Harbin Institute of Technology (HIT), Harbin, China, in 2021.

He is currently an Assistant Professor with the School of Electrical Engineering and Automation, HIT. From 2020 to 2021, he was a Visiting Ph.D. with the Technical University of Denmark. He has authored more than 20 journal papers in IEEE Transactions and held 9 authorized Chinese invention patents. His current research interests include advanced control of permanent magnet synchronous motor drives and electrolytic capacitorless ac motor drives.

Gaolin Wang (Senior Member, IEEE) received the B.S., M.S., and Ph.D. degrees in electrical engineering from Harbin Institute of Technology, Harbin, China, in 2002, 2004, and 2008 respectively.

In 2009, he was a Lecturer with the Department of Electrical Engineering, Harbin Institute of Technology, where he has been a Full Professor of Electrical Engineering since 2014. From 2009 to 2012, he was a Postdoctoral Fellow with Shanghai Step Electric Corporation, Shanghai, China. He has authored more than 70 technical papers published in IEEE Transactions. He is the holder of 40 Chinese patents. His current major research interests include permanent magnet synchronous motor drives and power converters.

Dr. Wang is currently a Guest Associate Editor for IEEE TRANSACTIONS ON INDUSTRIAL ELECTRONICS, and an Associate Editor of IEEE TRANSACTIONS ON TRANSPORTATION ELECTRIFICATION, *IET Electric Power Applications*.

Qiwei Wang (Member, IEEE) received the B.S., M.S., and Ph.D. degrees in electrical engineering from the Harbin Institute of Technology (HIT), Harbin, China, in 2015, 2017, and 2022, respectively.

He is currently an Assistant Professor with the School of Electrical Engineering and Automation, HIT. His current research interests include parameter identification technique, and PMSM position sensorless control.

Guoqiang Zhang (Senior Member, IEEE) received the B.S. degree in electrical engineering from Harbin Engineering University, Harbin, China, in 2011, and the M.S. and Ph.D. degrees in electrical engineering from Harbin Institute of Technology, Harbin, China, in 2013 and 2017, respectively.

Since 2017, he has been with the Department of Electrical Engineering, Harbin Institute of Technology, where he is currently an Associate Professor. His current research interests include control of electrical drives, and parameter identification technique, with main focus on sensorless field-oriented control of synchronous motor drives.

Dr. Zhang is currently an Associate Editor for *Journal of Power Electronics*.

Dianguo Xu (Fellow, IEEE) received the B.S. degree in control engineering from Harbin Engineering University, Harbin, China, in 1982, and the M.S. and Ph.D. degrees in electrical engineering from Harbin Institute of Technology (HIT), Harbin, China, in 1984 and 1989, respectively.

In 1984, he was an Assistant Professor with the Department of Electrical Engineering, HIT. Since 1994, he has been a Professor with the Department of Electrical Engineering, HIT. He was the Dean of the School of Electrical Engineering and Automation, HIT, from 2000 to 2010. He was the vice president of HIT, from 2014 to 2020. His research interests include renewable energy generation technology, power quality mitigation, sensorless vector controlled motor drives, high performance servo system. He published over 600 technical papers.

Dr. Xu is the Chairman of IEEE Harbin Section, Co-EIC of IEEE TRANSACTIONS ON POWER ELECTRONICS, an Associate Editor for IEEE TRANSACTIONS ON INDUSTRIAL ELECTRONICS, IEEE JOURNAL OF EMERGING AND SELECTED TOPICS IN POWER ELECTRONICS. He was the recipient of the 2018 IEEE IAS Outstanding Achievement Award.